RESEARCH ARTICLES
SPACE PHYSICS

Earth and Planetary Physics
2: 515–526, 2018
doi: 10.26464/epp2018050

Examples of unusual ionospheric observations by the CSES prior to earthquakes

Rui Yan*, XuHui Shen*, JianPing Huang, Qiao Wang, Wei Chu, DaPeng Liu, YanYan Yang, HengXin Lu, and Song Xu

The Institute of Crustal Dynamics, China Earthquake Administration, Beijing 100085, China

Abstract: The CSES (China seismic electromagnetic satellite) was launched on February 2, 2018 in a circular polar orbit at an altitude of ~507 km. One of the main objectives of CSES is to search for and characterize ionospheric perturbations that can be associated with seismic activities, to better understand the generation mechanism of such perturbations. Its scientific payload can measure a broad frequency range of electromagnetic waves and some important plasma parameters. This paper is a first-hand study of unusual observations recorded by the CSES over seismic regions prior to four earthquakes with M >7.0 since the satellite's launch. CSES detectors measured irregularities near the epicenter of these four earthquakes. It is already clear that data from instruments onboard the CSES will be of significant help in studies of characteristics of ionospheric perturbations related to earthquakes and their generation mechanisms.

Keywords: CSES; ionospheric perturbations; earthquake

Citation: Yan, R., Shen, X. H., Huang, J. P., Wang, Q., Chu, W., Liu, D. P., Yang, Y. Y., Lu, H. X., and Xu, S. (2018). Examples of unusual ionospheric observations by the CSES prior to earthquakes. *Earth Planet. Phys.*, *2*(6), 515–526. http://doi.org/10.26464/epp2018050

1. Introduction

Since the l980s, many countries have developed satellites capable of making electromagnetic observations. Spatial electromagnetic precursors to seismic events have been reported since then (Larkina et a1., 1983; Chmyrev et a1., 1989; Parrot and Mogilevsky, 1989; Molchanov et al., 1993), serving as a new observing technique for studying seismic electromagnetic effects (Zhang XM et al., 2009a). Many studies have focused on seismo-electromagnetic effects and disturbances in the ionosphere, and on possible generation mechanisms. The DEMETER satellite was the first satellite for earthquake monitoring from space (Parrot, 2006). It has provided data that has advanced research in this field.

Many ionospheric electromagnetic, plasma, and energy particle perturbations related to seismic activities have been detected. For the electromagnetic field, data in the range of ELF, VLF, and ULF frequencies have been studied. Zhang XM et al. (2009b) and Bhattacharya et al. (2007) found electric and magnetic field variations in the ULF/ELF range (40 Hz, 110 Hz, 350 Hz, and 400 Hz). Spectrogram results clearly indicate strong emissions before earthquakes. This is in agreement with the work done by Larkina et al. (1983), Bhattacharya and Gwal (2005) and Parrot et al. (2005), who earlier detected electromagnetic emissions over earthquake regions. Zeng ZC et al. (2009) and Zhu T and Wang LW (2011) studied average power spectrum density (APSD) of the electric field. In most cases, APSD in the range of ULF/ELF increased, while APSD in the range of VLF decreased. Zhu T and Wang LW (2011) also found that the amplitudes increased substantially before the occurrence of an earthquake. It then decreased and dropped almost to their minimum when the earthquake occurred. Akhoondzadeh et al. (2010) studied the cut-off frequency of the electromagnetic field. In their study, perturbations are observed near the epicenter of the quake in the form of change or transition in cut-off frequency at around 350–400 Hz range in ELF. The electric field is more prominent than the magnetic field spectrogram. For plasma observation data, the enhancement of both ionospheric plasma density and temperature are all found before the occurrence of earthquakes. Ion temperature, ion density, and electron density show uniform characteristics (Zhang XM et al., 2009c; Ouyang XY et al., 2011; Liu J, 2013; Liu J et al., 2014). GPS-TEC and f_oF_2 measurements have also been instrumental to improving the understanding of seismo-ionospheric variations, as demonstrated by Liu JY et al. (2002, 2004), Lognonné et al. (2006) and Ding ZH et al. (2010). Using IDP (an energetic particle detector) data from the French DEMETER satellite, Huang JP et al. (2010) analyzed energetic particles around the time of the M8.8 Chili earthquake and found increased night-time fluxes prior to the earthquake.

Statistical analyses have been used to study ionospheric parameters. Afonin et al. (1999) correlated ionospheric electron density perturbations and earthquakes, using data obtained by satellite Intercosmos 24 (Afonin et al., 1999). A statistical study of electric field variations up to 10 kHz (Němec et al., 2008, 2009) reported a statistically significant decrease of wave intensity several hours before the occurrence of an earthquake. Píša et al. (2012, 2013) arrived at the same conclusion using the complete DEMETER data set (9000 earthquakes) and found wave intensity decreases to a frequency of nearly 1.7 kHz during the nighttime. Zeren ZM et al. (2012) conducted statistical analysis of the characteristics of ELF/VLF disturbances of the magnetic field when M_s is greater

Correspondence to: R. Yan, yanxiaoxiao_best@163.com
X. H. Shen, shenxh@seis.ac.cn
Received 05 OCT 2018; Accepted 08 NOV 2018.
Accepted article online 28 NOV 2018.

than or equal to 7.0, based on northern hemisphere earthquakes occurring between 2005 and 2009. The authors found that for 42% of these earthquakes, perturbation amplitudes increased 30 days before the occurrence of an earthquake. For 35% of these earthquakes, however, decreased perturbation was observed. For the remaining 23%, no significant difference in perturbation was observed prior to the earthquake. Using a superposed epoch method, He Y et al. (2011) demonstrated that there is an increase of electron density close to the epicenter during night time. Statistical analyses have been performed using ion density peaks in the DEMETER data set (6.5 years) (Parrot, 2011, 2012; Li M and Parrot, 2012, 2013). The authors have shown that the number of good fits increases with the earthquake magnitude. In addition, it is found that the number of perturbations is higher for the day when earthquakes occur. Perturbations then slowly decrease after the earthquake. Yan R et al. (2017) found anomalous ionospheric perturbations related to earthquakes of magnitude larger than 5. The perturbations generally appear within a range of 200 km from the epicenter and mainly 5 days before the earthquakes. Using more than 6 years data observed in DEMETER, Zhang X et al. (2013) found that there are increases in the number of electron bursts prior to the events; during the entire operation period of the satellite, electron burst precipitation occurred before each strong earthquake with magnitude over 7.0. Liu JY et al. (2009) examined earthquakes during the 10-year period from 1 May 1998 to 30 April 2008 and performed a statistical analysis of GIM TEC and found that the GIM TEC above the epicenter decreased 3–5 days prior to the occurrence of 17 earthquakes with $M\geq 6.3$.

Both positive and negative ionospheric effects of these parameters are observed. According to the Lithosphere-Atmosphere-Ionosphere Coupling (LAIC) models, these effects can be explained by anomalous electric fields on the ground surface in either the positive or the negative direction (Pulinets, 2009). Analyses of ionospheric perturbations are provided by Hayakawa et al. (2004), Freund et al. (2009), Freund and Feeund (2015), Freund (2011), Pulinets et al. (2015), and De Santis et al. (2015). Ionospheric density variations could be triggered by changes of the electric field and currents in the global electric circuit between the bottom of the ionosphere and the Earth's surface, where electric charges occur, associated with stressed rocks (Kuo et al., 2011; Kelley et al., 2017). Other hypotheses and modeling can be found in monographs (Sorokin et al., 2015; Hayakawa, 2015), and references therein.

The China Seismo-Electromagnetic Satellite (CSES), which is also named as ZHANGHENG-1, was successfully launched on February 2, 2018 (Shen XH et al., 2018). The CSES is the first Chinese space-based platform for both earthquake observation and geophysical field measurement. It is the first satellite of the planned Chinese space-based geophysical field observation system and is expected to have a wide application in earthquake science, geophysics, space sciences, etc. The CSES can measure various physical parameters including electromagnetic field, electromagnetic waves, ionospheric plasma parameters, and high energy particles. One of its scientific objectives is to monitor and study ionospheric perturbations that appear to be associated with seismic activities, especially events of devastating size. The CSES is currently in its orbit-test phase. After the orbit-test, data obtained from the CSES will be published for public access (www.leos.ac.cn).

Although statistical analysis can help identify ionospheric changes associated with subsequent occurrence of earthquakes, studying individual earthquake events is important to the development of scientific understanding of these ionospheric variations. During the first few months of CSES operations, several earthquakes with $M>7.0$ were observed. The aim of this study is to present examples of ionospheric perturbations recorded by the various experiments carried by CSES when it was flying over active seismic regions during the orbit-test period. The scientific payload of the satellite and data recorded by the payload's various components are briefly described in Section 2. Analysis of data collected before, during, and after earthquakes is presented in Section 3, followed by discussion and conclusions in Section 4.

2. The CSES Satellite and Data Production

The CSES is a sun-synchronous satellite orbiting at a height of approximately 507 km with a descending node of 14:00 local time. The scientific payload of the CSES is composed of several instruments that provide a nearly continuous survey of ionospheric plasma, waves, and energetic particles. The EFD, an electric field detector, uses four electric probes to measure the three components of the electric field in a frequency range from DC up to 3.5 MHz. SCM, a search-coil magnetometer, measures the three components of the magnetic field in a frequency range from 10 Hz up to 20 kHz. The HPM, a high precision magnetometer, measures the vector of the Earth's magnetic field with a bandwidth from DC to 15 Hz. The LAP, a Langmuir probe, allows access to the electron density and temperature. The PAP, plasma analyzer package, measures ion density, composition, temperature, and flow velocity. The HEPP and Italian HEPD, high energetic particle package and detector, measure the proton energy spectrum, electron energy spectrum, and pitch angle. The GNSS-RO, GNSS occupation receiver, measures TEC, electron density, and atmosphere density. The TBB, tri-band beacon, measures TEC and electron density. Details about these instruments can be found in (Ambrosi et al., 2018; Cao JB et al., 2018; Cheng BJ et al., 2018; Lin J et al., 2018; Liu C et al., 2018; Huang JP et al.,2018; Chen L et al., 2018; Chu W et al.,2018; Yan R et al., 2018; Cheng Y et al., 2018).

During its five years' operation time, the CSES will acquire many kinds of data, e.g., multi-band waveform, spectrum of electric and-magnetic fields, in-situ plasma parameters (including densities and temperatures of electron and ion), electron density profiles and tomography, and energetic particle flux and energy spectra. There are five levels of data, which are described below:

Level-0: The raw data of payloads generated after a series of processings including frame synchronization, de-randomization, decoding, and de-formatting. All redundant data are removed in this level.

Level-1: The data obtained after general error rejection, format conversion, and calibration of Level-0 data.

Level-2: Physical quantity data with satellite orbit information after coordination system transformation and necessary data inversion of Level-1 data.

Level-3: Time sequential data in the frame of satellite orbits, gen-

erated after resampling and spectral analysis based on Level-2 data.

Level-4: Global or regional dynamic observation data retrieved from Level-2 and Level-3 data, in terms of variation between recursive orbits and disturbances observed according to comparison with the background field.

Experimenters and guest investigators can have access to the database and download data by application to their different authorities.

3. Data Analysis and Results

During August 2018, four earthquakes occurred with M>7.0 (Table 1), according to the report from China Earthquake Networks Center (http://www.ceic.ac.cn/speedsearch). We took these four earthquakes as examples. Based on their depths, these four earthquakes can be classified as shallow, intermediate depth, and deep. Their positions are shown in Figure 1.

Table 1. World earthquakes with M >7.0 in August 2018

M	Beijing Time	UTC	Lat. (°)	Lon. (°)	Depth (km)	Area
7.1	2018-08-29 11:51:54	2018-08-29 03:51:54	–21.95	170.10	20 Shallow	Ile Hunter, New Caledonia
7.3	2018-08-22 05:31:41	2018-08-21 21:31:41	10.76	–62.98	110 Intermediate	Rio Caribe, Venezuela
8.1	2018-08-19 08:19:37	2018-08-19 00:19:37	–18.08	–178.06	570 Deep	Ndoi Island, Fiji
7.1	2018-08-24 17:04:05	2018-08-24 9:04:05	–10.95	–70.75	600 Deep	Iberia, Peru

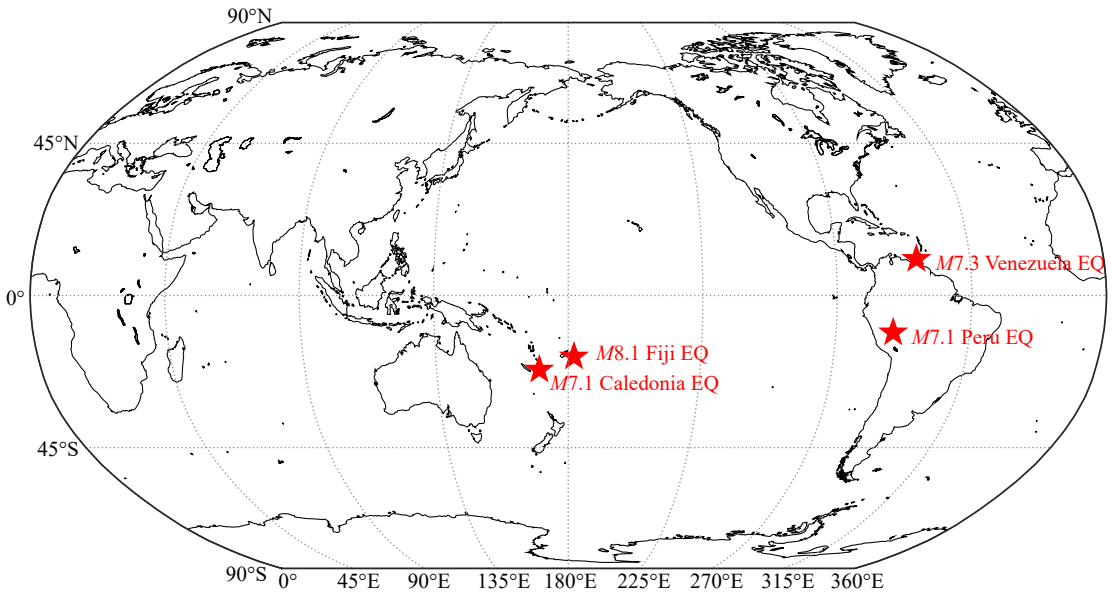

Figure 1. Location of the 4 earthquakes with M >7.0 in August.

Many geomagnetic disturbances, such as magnetic storms, could significantly disturb the ionosphere. In general, *Kp* index and *Dst* index can be used to determine whether a disturbance is caused by a space event or an earthquake. If the *Kp* index is less than or equal to 3, or the *Dst* index is greater than or equal to –20 nT, the period is considered to be quite geomagnetically calm. To separate seismo-ionospheric perturbations from geomagnetic fluctuations, *Dst* and *Kp* index are monitored. These indices are widely regarded as measures of solar wind-magnetosphere interaction and are used in examining interplanetary and solar phenomena (Sarkar et al., 2007). *Kp* index and *Dst* index data related to solar activities and geomagnetic conditions during August, 2018, are shown in Figure 2. Evidence of a severe magnetic storm from 25 August to 28 August is apparent.

Observation data from the satellite's EFD, SCM, LAP, PAP and HEPP associated with these four earthquakes are studied and discussed below.

3.1 Case-I: Shallow Depth Earthquake

The first seismic event discussed in this paper is the Hunter earthquake, a shallow event that occurred about 300 km to the east of the island of New Caledonia in the southwest Pacific Ocean on August 29, 2018 at 03:51:54 UT. The magnitude of this earthquake is 7.1 and the depth is 20 km. The epicenter is located at geographic 21.95°S and 170.10°E. The revisited orbits close (less than 1000 km) to the epicenter are shown in Figure 3, in which the star indicates the epicenter of the quake. Panel (a) of Figure 3 corresponds to ascending orbits (nighttime), and the right panel (b) is for descending orbits (daytime). The blue curves represent footprints of the revisited orbits; the numbers near these curves indicate orbit number and time (date). For instance, in the number combination "31371-0827", '3137' is the orbit number, '1' is the sub-orbit (in this case, ascending orbit); '0827' means 27th August.

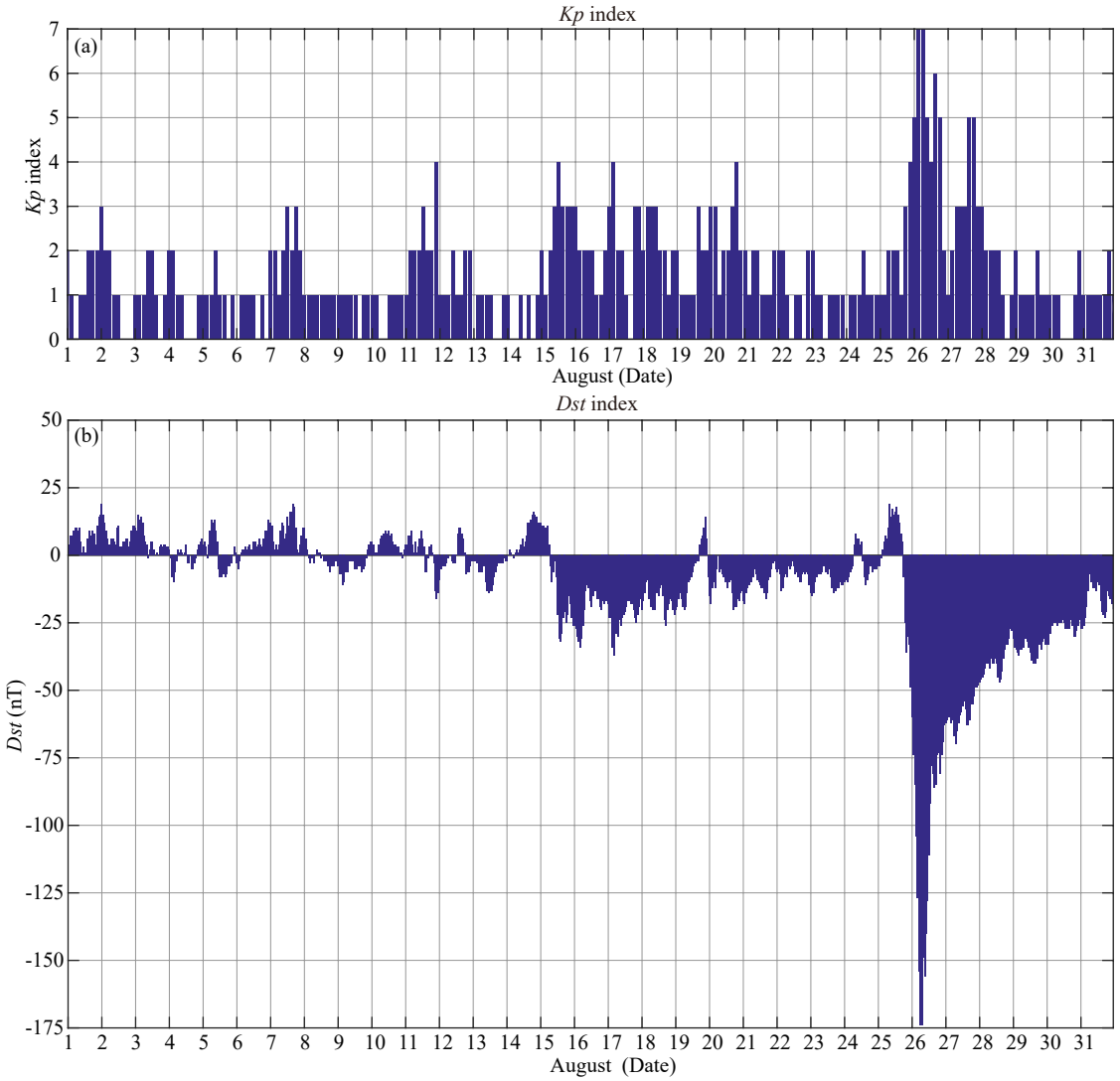

Figure 2. Magnetic activity conditions during August.

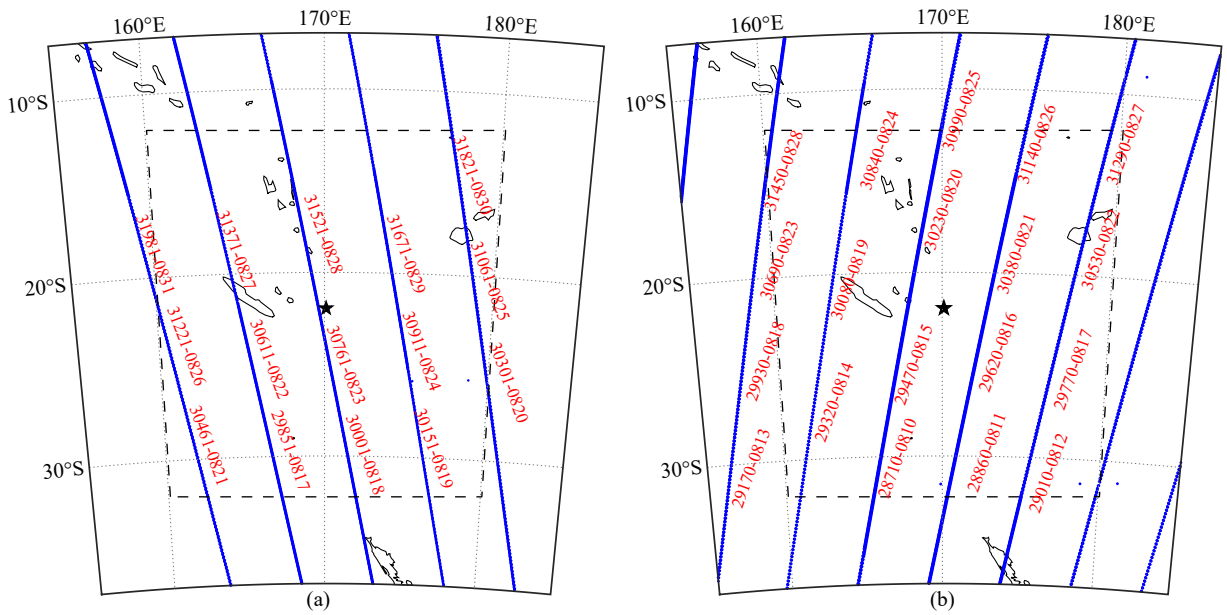

Figure 3. The distribution of revisited orbits close (less than 1000 km) to the epicenter. (a) Ascending orbits; (b) Descending orbits.

We used space difference methods (Liu, 2013) to analyze the nighttime electron density (N_e) observed by the LAP. Taking the epicenter as center, a ±15° area was divided into grids of 4° (longitude) × 2° (latitude). The background average (*Ab*) and standard deviation (σ) in each grid were then obtained using data collected in July. From 12 days prior to EQs to 2 days after EQs, averaged observation data (*Ao*) for each orbit inside each grid are obtained. The normalization can be calculated from the ratio of (*Ao*−*Ab*) and σ in each grid. Space difference results are shown in Figure 4, in which ±10σ (standard deviation) was selected as the threshold for abnormity. The nighttime N_e space differences observed during August 17–31 are shown. *X*-axis and *Y*-axis are longitude and latitude respectively. The threshold of the difference is color-coded according to the scale on the bottom. The star represents the epicenter. Panels (a), (b), and (c) correspond to the following time intervals: August 17–21, 22–26, and 27–31.

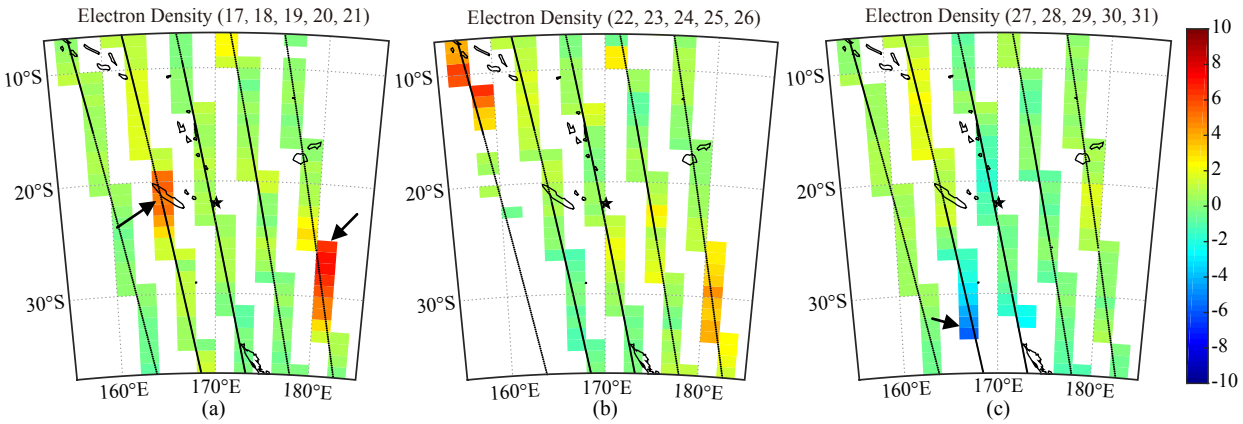

Figure 4. N_e space difference near to the epicenter of the Hunter Earthquake (less than 15°)

However, a severe magnetic storm began on August 25 and lasted until August 27. The *Dst* and *Kp* indexes are large during these days. So it is difficult to distinguish whether the perturbation is caused by the magnetic storm or the earthquake. We found an intense enhancement on August 20 and an enhancement on August 17 (arrow in Figure 4a). These two increases appear before the earthquake and are near to its epicenter. Although the date of August 17, *Kp* index is equal to 4 during 03:00–06:00 UT, the date time passing by epicenter is around 15:00–15:30 UT where *Kp* is equal to 2. Hence the enhancement occurred on the 17th and 20th August is probably related to the Hunter Earthquake. The increases in Figure 4b that occurred on the 25th and 26th August are probably related to the magnetic storm. There is a decrease on August 27 (Figure 4c), two days before earthquake. Some abnormal increases are also found in the proton spectrum observed by the HEPP prior to the earthquakes. Data of all revised orbits near the epicenter (less than 10°) are compared and a significant increase is found. As shown in Figure 5, compared to data from other revisited orbits, on August 18 a significant electron flux increase is observed at almost all telescopes (it is not significant in the data from telescopes 1 and 9). Results of data from telescopes 4 and 5 are shown in Figure 5, in which the *X*-axis is latitude and the *Y*-axis is electron flux. Lines in different colors represent different orbits, orbits 29241, 30001, 30761, and 31521 (Figure 3a). The *Kp* index on August 18 is at its minimum and the position is in the middle latitude, which is not affected by the aurora zone.

Anomalies in the magnetic field in some frequency ranges were also observed. Based on previous research (Zhang XM et al. 2009b; Bhattacharya et al., 2007; Zeng ZC et al., 2009; Zhu T and Wang LW et al., 2011), most abnormal magnetic field seismic signals observed by satellite are in a frequency range of DC –1000 Hz. The power spectrum density (PSD) in this frequency range has been, therefore, further studied. Similar to the space difference method, nighttime revisited orbits which are less than 30° from epicenter are identified for further analyses. Data from 10 days to 40 days before the occurrence of the earthquake are used as background. The ±30° area was divided into grids of 5° (longitude) × 2.5° (latitude). Average background average (*Ab*) in each grid was then obtained. The average values of observe data (*Ao*) in every 5 days using data 15 days prior to the EQs are also calculated. The difference between *Ao* and *Ab* is shown in Figure 6.

Figure 6 displays the PSD difference of a magnetic component (E_z) at the 500 Hz frequency during August 15–19 (Figure 6a), 20–24 (Figure 6b), and 25–29 (Figure 6c). PSD difference is color coded according to the scale at the bottom. The star represents the event's epicenter. An increasing trend in Figure 6c is observed, which is most probably caused by the magnetic storm. In addition, the revisited orbits that passed by the epicenter are during 14:00–15:30 UT. The *Kp* index values larger than 3 occur at 13:00–15:00 on August 15, at 4:00–6:00 in August 17, and at 19:00–21:00 in August 20. Considering these times and positions when the *Kp* index is large than 3, the increases observed to the southwest of the epicenter (arrow in Figure 6a) are probably due to the earthquake. The increases occurred on August 17 and 18.

The spectrum of the electric field in the range of DC–2.5 kHz was analyzed. First we calculate accumulation of power spectrum density (PSD) in each nighttime orbit within 10° of the epicenter. The time sequence of these accumulation values during August 10–28 along the frequency spectrum are shown in Figure 7, in which the *X*-axis is date and the *Y*-axis is frequency. The PSD accumulation value is color-coded according to the scale on the right. The panels from top to bottom correspond to the E_x, E_y, and E_z components of electric field. It can be seen that there is a strong

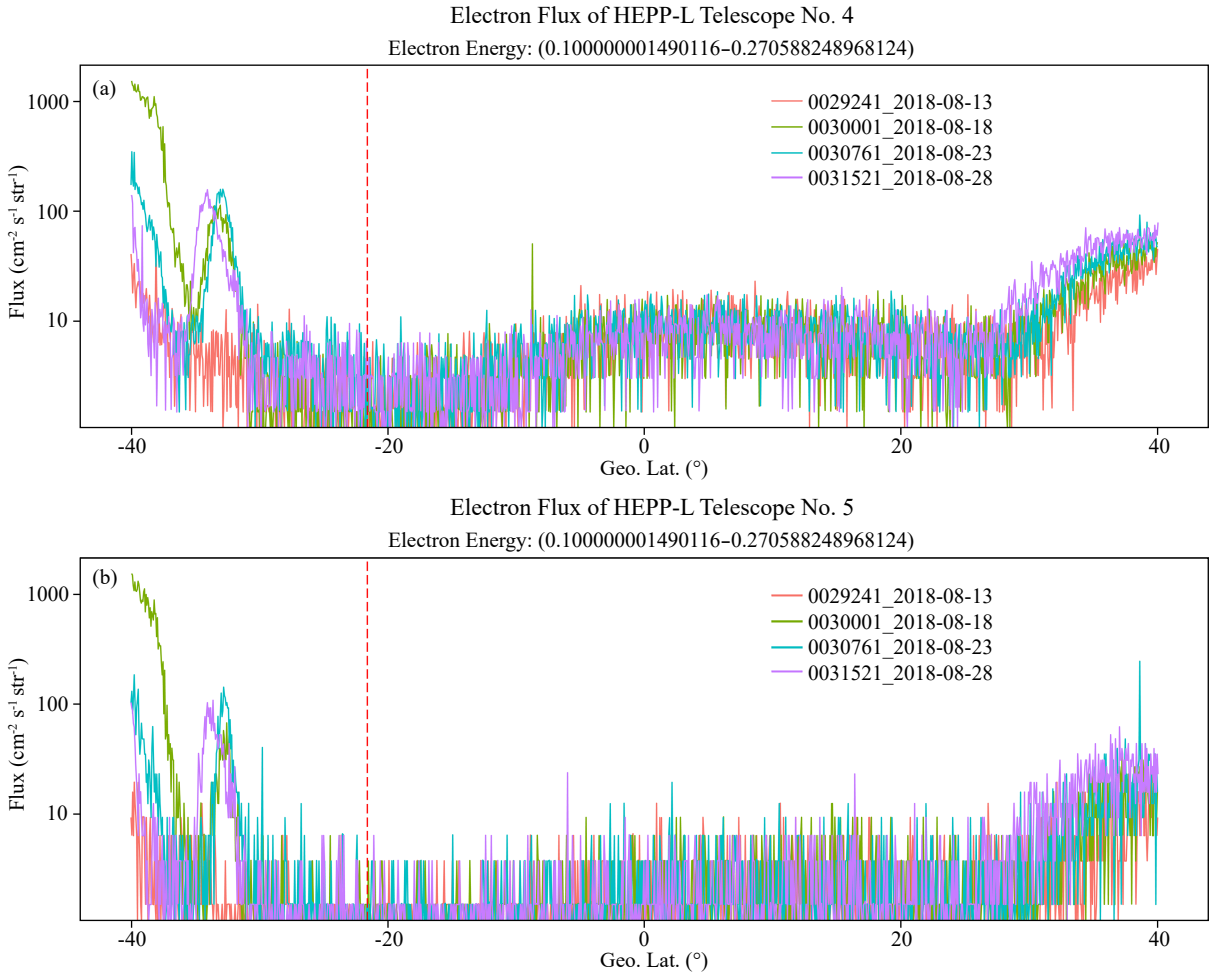

Figure 5. Proton spectrum observed by HEPP-L. (a) Telescope 4; (b) Telescope 5.

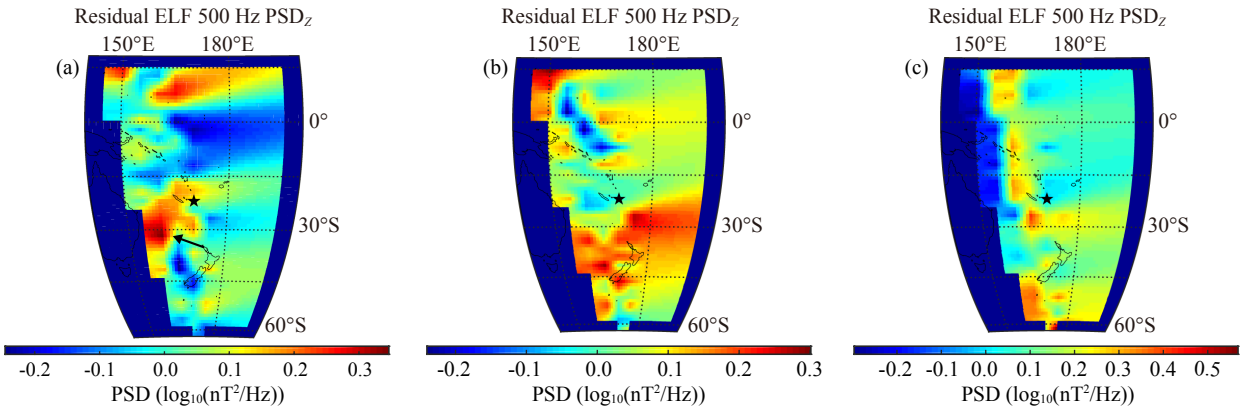

Figure 6. The *Z* component magnetic field PSD difference at 500 Hz. (a) August 15–19; (b) August 20–24; (c) August 25–29.

increment of PSD near 7 kHz and below 5 kHz on August 18; a weak increment for all three components is observed on August 28. Magnetic activity conditions are rather quiet on those two days. It is noted that in the E_x direction there are obvious increases on August 11, 16, 21, and 26 in the 0 to 25 kHz range. They appear in the revisited orbits, which means that in the same area the PSD remains high.

3.2 Case-II: Intermediate Depth Earthquake

An *M* 7.3 earthquake of intermediate depth occurred at 21:31:41 on August 21, 2018, 23 km from Rio Caribe, Venezuela. Its epicenter was at 10.76°N, 62.98°W and its depth was 110 km.

Ionospheric perturbations of N_e within 10 days before and 2 days after this earthquake were studied, using the moving average method. The nighttime data collected on one orbit within ±10°

around the epicenter were resampled by 0.5° in the direction along the latitude. The background average value (*Ab*) and standard deviation (σ) were calculated using data from the previous 10 orbits (about 10 days), taking $Ab\pm2\sigma$ as the upper and lower thresholds. The average value of current resampled orbit data (*Ao*) is also shown at the same time (upper panel Figure 8). The relat-

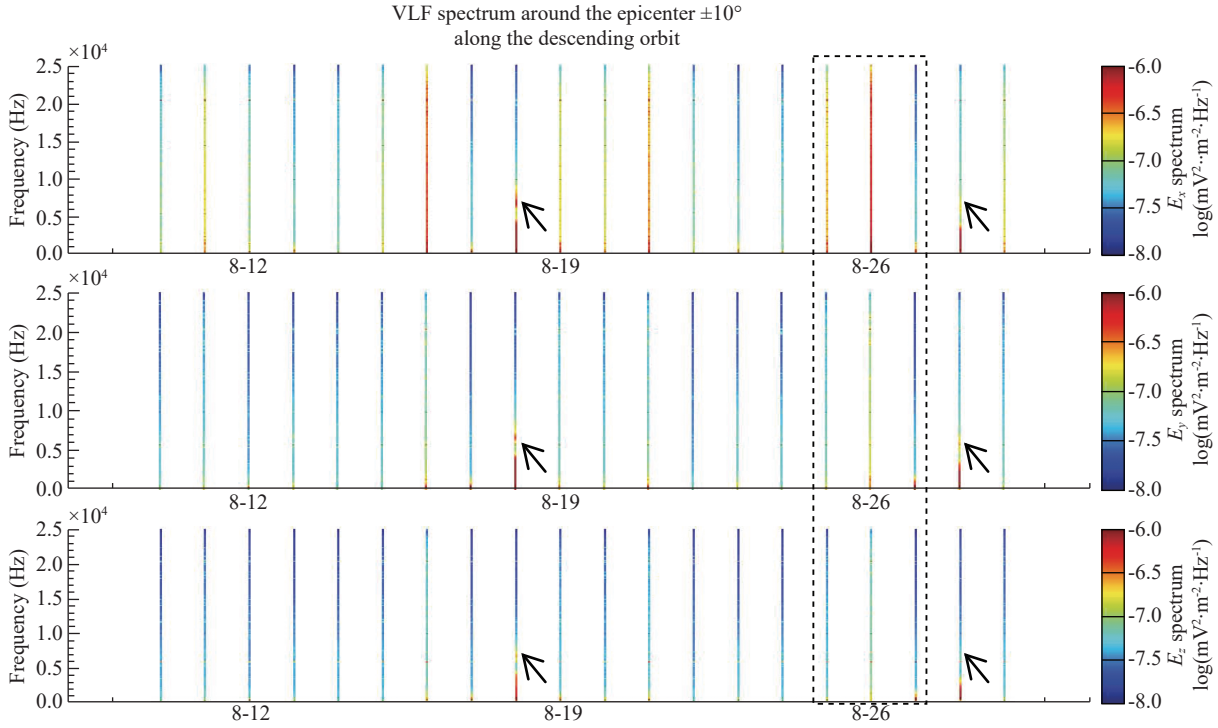

Figure 7. The time sequence of PSD accumulation of in each orbit before earthquake *M* 7.1 occurred in August 29.

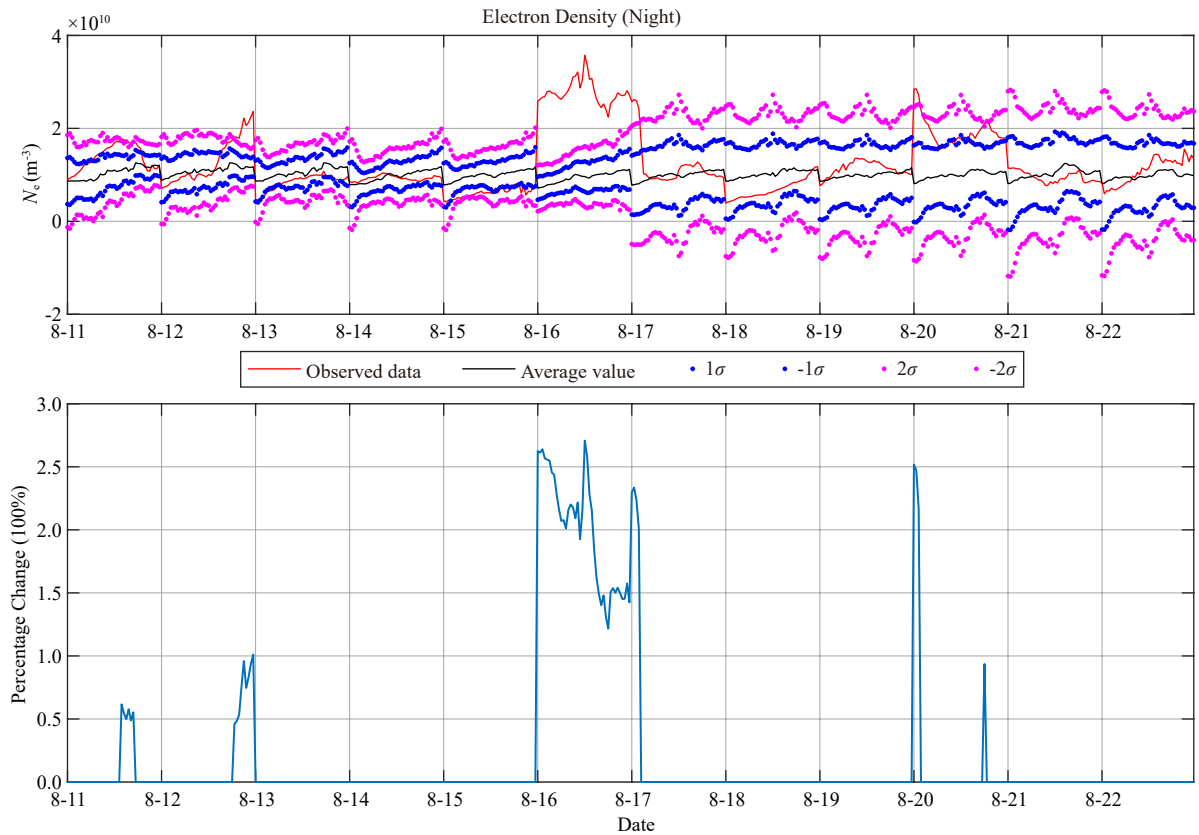

Figure 8. The time series analysis of N_e moving average value.

ive change $(Ao–Ab)/\sigma$ is calculated when observation value is greater than the upper threshold or smaller than the lower threshold. If observation values are between the upper and lower thresholds, the relative change is then 0 (bottom panel Figure 8).

The upper panel of Figure 8 shows the variations in observed N_e, background, and upper and lower thresholds (from August 11 to August 22), including during the earthquake (August 21). Increases on August 12 and August 16 are obvious. The variation for August 16 is more than 2σ. The *Kp* index during these revisited orbits concentrates on the time interval of 05:00–07:00 and is consistently less than or equal to 3. Hence, the two N_e increases observed 5 days (August 16) and 9 days (August 12) before the earthquake are not due to magnetic storms. The increases observed on August 11 and August 20 were single points, not enough to be considered anomalies.

Disturbances on August 16 were observed also by the PAP: significant increases of oxygen density (N_{O+}) and ion longitudinal drift velocity (V_x). These two parameters showed rapid increases in the region of 100 km above the epicenter; observed values drop significantly when the satellite leaves the epicenter region (Figure 9).

Similar to Figure 6, Figure 10 displays differences in the PSD-measured magnetic component (E_z) at 500 Hz during August 7–11 (Figure 10a), 12–16 (Figure 10b), and 17–21 (Figure 10c). PSD differences are color coded according to the scale at the bottom. The star indicates the epicenter. As the earthquake is approaching, the PSD close to the epicenter is observed to increase. In particular, to the east of the epicenter, the PSD increased to its maximum 0–5 days before the earthquake. However, it is noted that the position of increase is around the position of the orbit 29791 (August 17), as shown in Figure 11. The *Kp* index is 4 at 03:00–06:00 on August 17. Orbit No. 29791 passed by the epicenter at approximately 05:30 UT. Therefore, it is reasonable to argue that such an in-

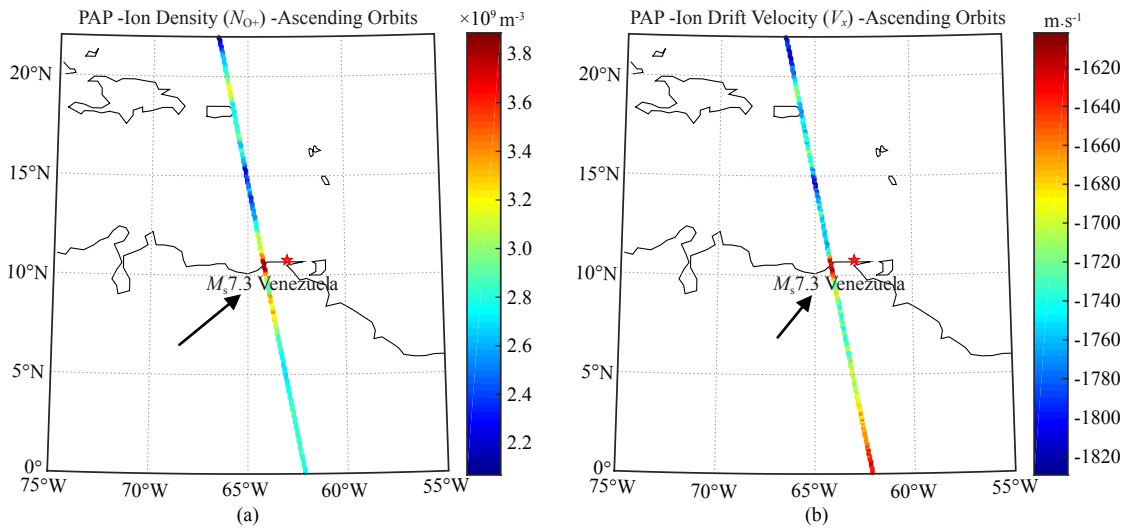

Figure 9. Abnormal phenomena observed by the PAP. (a) N_{O+}; (b) V_x.

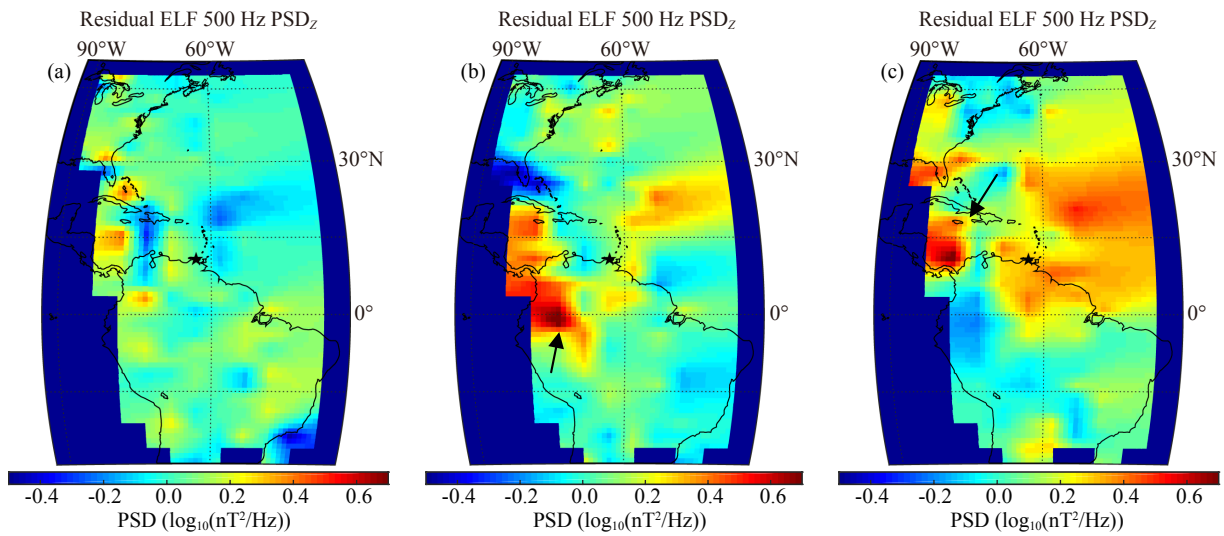

Figure 10. The magnetic field *Z* component PSD difference at 500 Hz. (a) August 7–11; (b) August 12–16; (c) August 17–21.

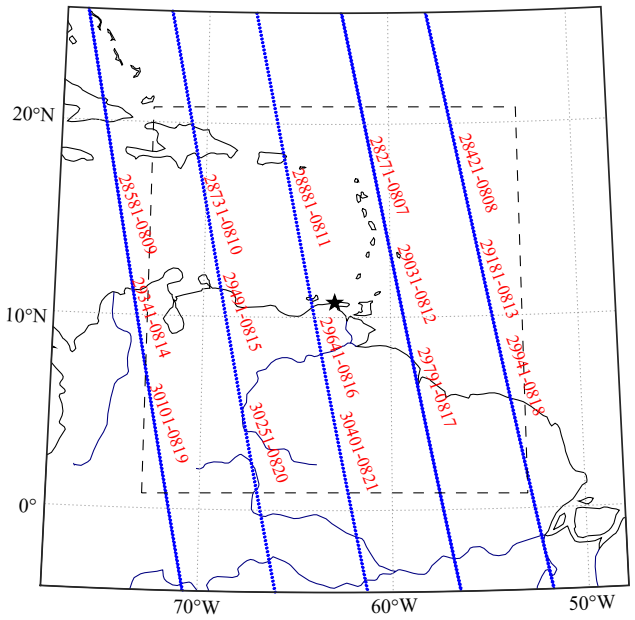

Figure 11. The ascending revisited orbits close to the epicenter (less than 10°).

crease is related to magnetic activities. The increase on August 15 (Figure 10b and Figure 11) and the one on August 20 (Figure 10c and Figure 11) are more likely related to the earthquake. These increments are all to the west of the epicenter (arrows in Figure 10).

3.3 Case-III: Deep Depth Earthquakes

The first deep seismic event observed is the earthquake close to 138 km WNW of Iberia, Peru, which occurred on August 24, 2018, at 09:04:05 UT. The magnitude of this earthquake was 7.1, the depth is 600 km and the epicenter was located at geographic 10.95°S and 70.75°W. Similarly, the data of revisited orbits close (less than 1000 km) to the epicenter are identified.

Similar to Figure 7, the electric field spectrum in the range of DC–2.5 kHz was analyzed. The time sequence of observed values accumulated along the spectrum during August 10–19 is shown in Figure 12. An anomalous increment of PSD below 15 kHz is obvious on August 18. The increase is found in all three components. The magnetic activity condition on this day was quiet.

The fourth case study is a deep earthquake of magnitude 8.1 that occurred on August 19, 2018 at 00:19:37 UT close to Ndoi Island, Fiji (18.08°S, 178.06°W). For the proton spectrum observed by HEPP, we first calculate the background spectrum average value using revisited orbit data collected between 21 July and 19 August near the epicenter (less than 10°). The spectrum 0–5 days before the earthquake is then calculated (Figure 13). In Figure 13, the *X*-axis is the energy and the *Y*-axis is the proton spectrum flux. The blue curve displays background data collected from 21 July to 19 August. The red curve displays observations from 15 to 19 August, before the earthquake, showing that, compared to the relatively calm background spectrum, the proton energy spectrum in these days immediately prior to the earthquake was significantly disturbed.

Accumulated power spectrum densities (PSD) of the electric field for each nighttime orbit within 10° around the epicenter are also analyzed (Figure 14). An increment of PSD in the range of 10 kHz–20 kHz on 17 August (ellipse in Figure 14) is observed. The increase is shown in all three E_x, E_y, E_z components. The *Kp* index is found to be minimum.

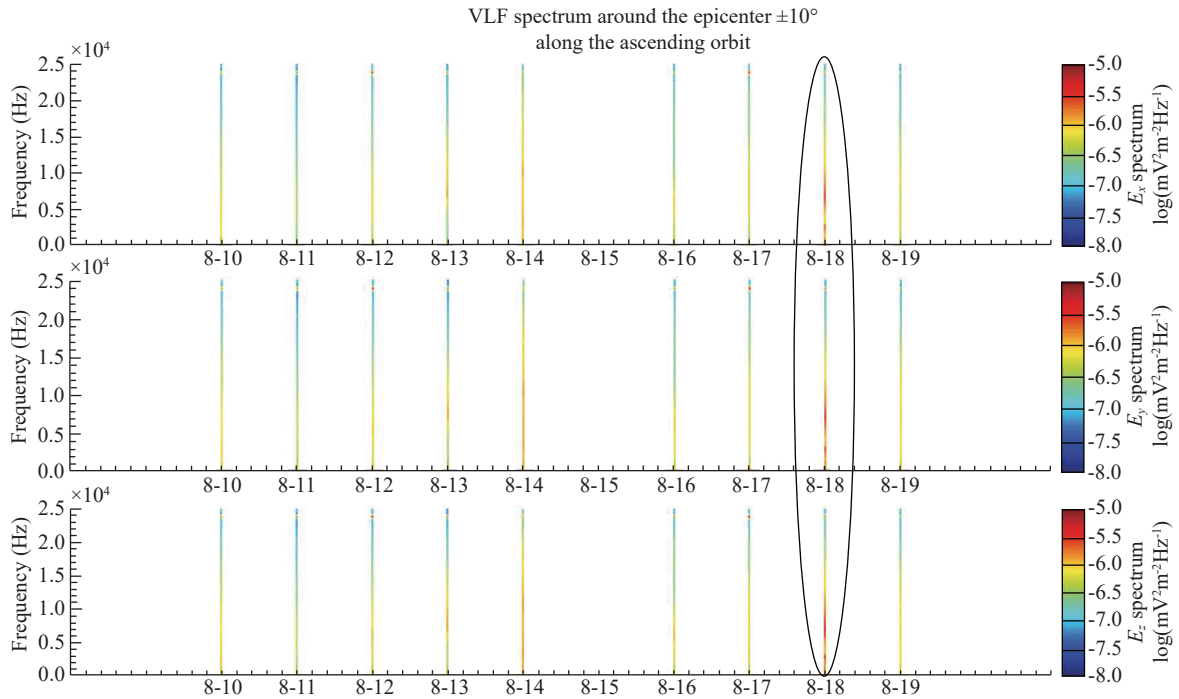

Figure 12. The time sequence of PSD accumulation of in each orbit before earthquake.

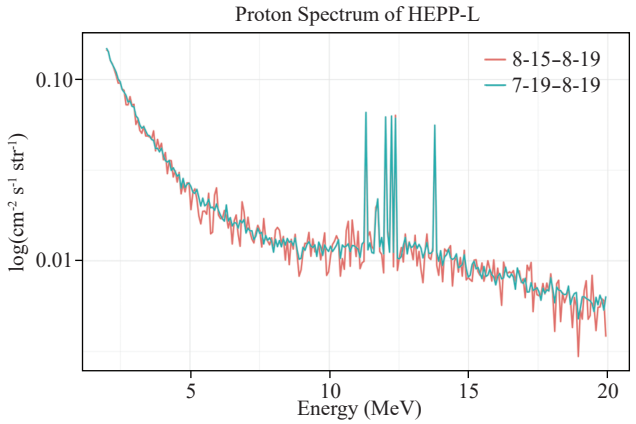

Figure 13. The variation of electron Spectrum spectrum observed by HEPP-L.

4. Discussion and Conclusions

This study presents ionospheric perturbations observed during four earthquakes. These perturbations were recorded by the CSES's EFD, SCM, LAP, PAP and HEPP instruments. These results demonstrate that unusual features in waves, plasma, and energetic particle fluxes can be recorded when the satellite flies over regions that include epicenters of future earthquakes. All phenomena related to earthquakes in this study were observed during nighttime orbits. The deeper the earthquake depth, the fewer were the anomalous phenomena observed. The greater were the magnitude of the seismic disturbance, the greater the observed electromagnetic disturbances.

Conclusions from this study can be summarized as follows:

(1) The same parameters may not be reflected in each earthquake, and the observed anomalies may not be the same as in previous events.

(2) Perturbations of different parameters can occur at various locations and times.

(3) The time and location of disturbances before an earthquake appear to vary from one event to another.

(4) Perturbations are found for some parameters after earthquakes, but not for every parameter in each earthquake.

All the measured parameters display similar background variations in absence of seismic activity since the ionosphere is affected by a number of other factors. *Kp* and *Dst* can be used to examine whether perturbations are from earthquakes or magnetic storms, but they cannot be used to rule out other possibilities. This is one of the challenges in studying earthquake precursors.

Based on results presented in this study, we conclude that CSES data are responsive to earthquake events. As the CSES becomes fully operational, it will facilitate detailed study of the relationship between ionospheric perturbations and earthquakes. Additional case studies will further advance understanding and predicting earthquake activity.

Acknowledgments

This work was supported by the National Natural Science Foundation of China (41404058). We thank GFZ for providing *Kp* index data (https://www.gfz-potsdam.de/en/kp-index/) and World Data Center for Geomagnetism for *Dst* index data (http://wdc.kugi.kyoto-u.ac.jp/dst_realtime/index.html).

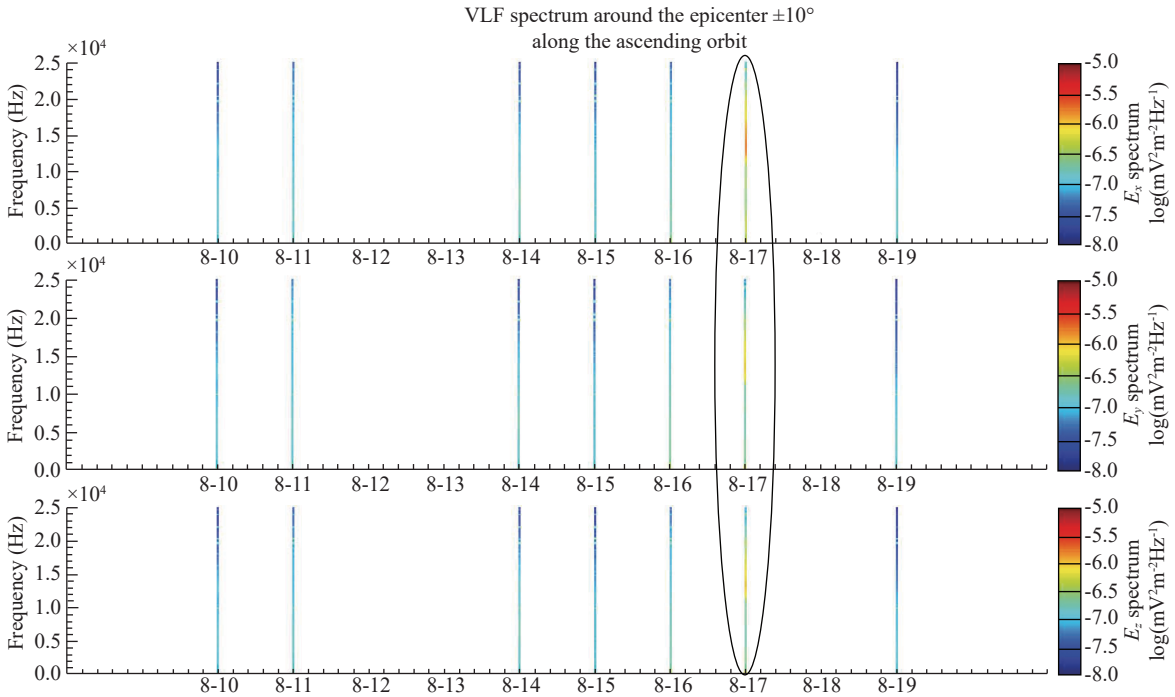

Figure 14. The time sequence of PSD accumulation for each orbit before earthquake.

References

Afonin, V. V., Molchanov, O. A., Kodama, T., Hayakawa, M., and Akentieva, O. A. (1999). Statistical study of ionospheric plasma response to seismic activity: Search for reliable result from satellite observations. In Hayakawa, M. (Ed.), *Atmospheric and Ionospheric Electromagnetic Phenomena Associated with Earthquakes* (pp. 597–617). Tokyo, Japan: Terra Scientific Publishing Company.

Akhoondzadeh, M., Parrot, M., and Saradjian, M. R. (2010). Investigation of VLF and HF waves showing seismo-ionospheric anomalies induced by the 29 September 2009 Samoa earthquake (M_w=8.1). *Nat. Hazards Earth Syst. Sci.*, *10*(5), 1061–1067. https://doi.org/10.5194/nhess-10-1061-2010

Ambrosi, G., Bartocci, S., Basara, L., Battiston, R., Burger, W. J., Carfora, L., Castellini, G., Cipollone, P., Conti, L., … Vitale, V. (2018). The HEPD particle detector of the CSES satellite mission for investigating seismo-associated perturbations of the Van Allen belts. *Sci. China Technol. Sci.*, *61*(5), 643–652. https://doi.org/10.1007/s11431-018-9234-9

Bhattacharya, S., and Gwal, A. K. (2005). Observations made by DEMETER micro-satellite for ultra low frequency and extremely low frequency emissions during Indonesian earthquake. In *Proceedings of XXXVIII General Assembly of International Union of Radio Science*. India.

Bhattacharya, S., Sarkar, S., Gwal, A. K., and Parrot, M. (2007). Satellite and ground-based ULF/ELF emissions observed before Gujarat earthquake in March 2006. *Curr. Sci.*, *93*(1), 41–46.

Cao, J. B., Zeng, L., Zhan, F., Wang, Z. G., Wang, Y., Chen, Y., Meng, Q. C., Ji, Z. Q., Wang P. F., … Ma, L. Y. (2018). The electromagnetic wave experiment for CSES mission: Search coil magnetometer. *Sci. China Technol. Sci.*, *61*(5), 653–658. https://doi.org/10.1007/s11431-018-9241-7

Cheng, B. J., Zhou, B., Magnes, W., Lammegger, R., and Pollinger, A. (2018). High precision magnetometer for geomagnetic exploration onboard of the China Seismo-Electromagnetic Satellite. *Sci. China Technol. Sci.*, *61*(5), 659–668. https://doi.org/10.1007/s11431-018-9247-6

Chen, L., Ou, M., Yuan, Y. P., Sun, F., Yu, X., and Zhen, W. M. (2018). Preliminary observation results of the Coherent Beacon System onboard the China Seismo-Electromagnetic Satellite-1. *Earth Planet. Phys.*, *2*(6), 505–514. https://doi.org/10.26464/epp2018049

Chmyrev, V. M., Isaev, N. V., Bilichenko, S. V., and Stanev, G. (1989). Observation by space-borne detectors of electric fields and hydromagnetic waves in the ionosphere over an earthquake center. *Phys. Earth Planet. Interi.*, *57*(1–2), 110–114. https://doi.org/10.1016/0031-9201(89)90220-3

Cheng, Y., Lin, J., Shen, X. H., Wan, X., Li, X. X., and Wang, W. J. (2018). Analysis of GNSS radio occultation data from satellite ZH-01. *Earth Planet. Phys.*, *2*(6), 499–504. https://doi.org/10.26464/epp2018048

Chu, W., Huang, J. P., Shen, X. H., Wang, P., Li, X. Q., An, Z. H., Xu, Y. B., and Liang, X. H. (2018). Preliminary results of the High Energetic Particle Package on-board the China Seismo-Electromagnetic Satellite. *Earth Planet. Phys.*, *2*(6), 489–498. https://doi.org/10.26464/epp2018047

De Santis A., De Franceschi, G., Spogli, L., Perrone, L., Alfonsi, L., Qamili, E., Cianchini, G., Di Giovambattista, R., Salvi, S., … Tao, D. (2015). Geospace perturbations induced by the Earth: the state of the art and future trends. *Phys. Chem. Earth*, *85–86*, 17–33. https://doi.org/10.1016/j.pce.2015.05.004

Ding, Z. H., Wu, J., Su, S. J., Chen, J. S., and Ban, P. P. (2010). The variation of ionosphere on some days before the Wenchuan Earthquake. *Chinese J. Geophys.* (*in Chinese*), *53*(1), 30–38. https://doi.org/10.3969/j.issn.0001-5733.2010.01.004

Freund, F. (2011). Pre-earthquake signals: Underlying physical processes. *J. Asian Earth Sci.*, *41*(4–5), 383–400. https://doi.org/10.1016/j.jseaes.2010.03.009

Freund, F. T., Kulahci, I. G., Cyr, G., Ling, J. L., Winnick, M., Tregloan-Reed, J., and Freund, M. M. (2009). Air ionization at rock surfaces and pre-earthquake signals. *J. Atmos. Sol. Terr. Phys.*, *71*(17–18), 1824–1834. https://doi.org/10.1016/j.jastp.2009.07.013

Freund, F. T., and Freund, M. M. (2015). Paradox of peroxy defects and positive holes in rocks. Part Ⅰ: Effect of temperature. *J. Asian Earth Sci.*, *114*, 373–383. https://doi.org/10.1016/j.jseaes.2015.04.047

Hayakawa, M., Molchanov, O. A., and NASDA/UEC team. (2004). Summary report of NASDA's earthquake remote sensing frontier project. *Phys. Chem. Earth*, *29*(4–9), 617–625. https://doi.org/10.1016/j.pce.2003.08.062

Hayakawa, M. (2015). Earthquake Prediction with Radio Techniques (pp. 294). Singapore: John Wiley & Sons.

He, Y., Yang, D., Qian, J., and Parrot, M. (2011). Response of the ionospheric electron density to different types of seismic events. *Nat. Hazards Earth Syst. Sci.*, *11*(8), 2173–2180. https://doi.org/10.5194/nhess-11-2173-2011

Huang, J. P., Liu, J., Ouyang, X. Y., and Li, W. J. (2010). Analysis to the energetic particles around the *M*8.8 Chili earthquake. *Seismol. Geol.* , *32*(3), 417–423. https://doi.org/10.3969/j.issn.0253-4967.2010.03.008

Huang, J. P., Lei, J. G., Li, S. X., Zeren, Z. M., Li, C., Zhu, X. H., and Yu, W. H. (2018). The Electric Field Detector (EFD) onboard the ZH-1 satellite and first observational results. *Earth Planet. Phys.*, *2*(6), 469–478. https://doi.org/10.26464/epp2018045

Kelley, M. C., Swartz, W. E., and Heki, K. (2017). Apparent ionospheric total electron content variations prior to major earthquakes due to electric fields created by tectonic stresses. *J. Geophys. Res.*, *122*(6), 6689–6695. https://doi.org/10.1002/2016JA023601

Kuo, C. L., Huba, J. D., Joyce, G., and Lee, L. C. (2011). Ionosphere plasma bubbles and density variations induced by pre-earthquake rock currents and associated surface charges. *J. Geophys. Res.*, *116*(A10), A10317. https://doi.org/10.1029/2011JA016628

Larkina, V. I., Nalivayko, A. V., Gershenzon, N. I., Gokhberg, M. B., Liperovskiy, V. A., and Shalimov, S. L. (1983). Observations of VLF emission, related with seismic activity, on the Interkosmos-19 satellite. *Geomagn. Aeron.* (*Engl. Transl.*), *23*(5), 684–687.

Li, M., and Parrot, M. (2012). "Real time analysis" of the ion density measured by the satellite DEMETER in relation with the seismic activity. *Nat. Hazards Earth Syst. Sci.*, *12*(9), 2957–2963. https://doi.org/10.5194/nhess-12-2957-2012

Li, M., and Parrot, M. (2013). Statistical analysis of an ionospheric parameter as a base for earthquake prediction. *J. Geophys. Res.*, *118*(6), 3731–3739. https://doi.org/10.1002/jgra.50313

Liu, J. (2013). Ionopheric perturbance study before earthquakes (in Chinese). Beijing: Chinese Academy of Sciences.

Lin, J., Shen, X. H., Hu, L. C., Wang, L. W., and Zhu, F. Y. (2018). CSES GNSS ionospheric inversion technique, validation and error analysis. *Sci. China Technol. Sci.*, *61*(5), 669–677. https://doi.org/10.1007/s11431-018-9245-6

Liu, C., Guan, Y. B., Zheng, X. Z., Zhang, A. B., Piero, D., and Sun, Y. Q. (2018). The technology of space plasma in-situ measurement on the China Seismo-Electromagnetic Satellite. *Sci. China Technol. Sci.*. https://doi.org/10.1007/s11431-018-9345-8

Liu, J., Huang, J. P., and Zhang, X. M. (2014). Ionospheric perturbations in plasma parameters before global strong earthquakes. *Adv. Space Res.*, *53*(5), 776–787. https://doi.org/10.1016/j.asr.2013.12.029

Liu, J. Y., Chuo, Y. J., Pulinets, S. A., Tsai, H. F., and Zeng, X. P. (2002). A study on the TEC perturbations prior to the Rei-Li, Chi-Chi and Chia-Yi earthquakes. In Hayakawa, M., and Molchanov, O. A. (Eds.), *Seismo-Electromagnetics: Lithosphere-Atmosphere-Ionosphere Coupling* (pp. 297–301). Tokyo: TERRRAPUB.

Liu, J. Y., Chuo, Y. J., Shan, S. J., Tsai, Y. B., Pulinets, S. A., and Yu S. B. (2004). Pre-earthquake ionospheric anomalies registered by continuous GPS TEC measurements. *Ann. Geophys.*, *22*(5), 1585–1593. https://doi.org/10.5194/angeo-22-1585-2004

Liu, J. Y., Chen, Y. I., Chen, C. H., Liu, C. Y., Chen, C. Y., Nishihashi, M., Li, J. Z., Xia, Y. Q., Oyama, K. I., … Lin, C. H. (2009). Seismoionospheric GPS total electron content anomalies observed before the 12 May 2008 M_w7.9 Wenchuan earthquake. *J. Geophys. Res.*, *114*(A4), A04320. https://doi.org/10.1029/2008JA013698

Lognonné, P., Artru, J., Garcia, R., Crespon, F., Ducic, V., Jeansou, E., Occhipinti, G., Helbert, J., Moreaux, G., and God P. E. (2006). Ground-based GPS imaging of ionospheric post-seismic signal. *Planet. Space Sci.*, *54*(5), 528–540. https://doi.org/10.1016/j.pss.2005.10.021

Molchanov, O. A., Mazhaeva, O. A., Golyavin, A. N., and Hayakawa, M. (1993). Observation by the Intercosmos-24 satellite of ELF-VLF electromagnetic emissions associated with earthquakes. *Ann. Geophys.*, *11*(5), 431–440.

Němec, F., Santolík, O., Parrot, M., and Berthelier, J. J. (2008). Spacecraft

observations of electromagnetic perturbations connected with seismic activity. *Geophys. Res. Lett.*, *35*(5), L05109. https://doi.org/10.1029/2007GL032517

Němec, F., Santolík, O., and Parrot, M. (2009). Decrease of intensity of ELF/VLF waves observed in the upper ionosphere close to earthquakes: a statistical study. *J. Geophys. Res.*, *114*(A4), A04303. https://doi.org/10.1029/2008JA013972

Ouyang, X. Y., Zhang, X. M., Shen, X. H., Huang, J. P., Liu, J., Zeren, Z. M., and Zhao, S. F. (2011). Disturbance of O^+ density before major earthquake detected by DEMETER satellite. *Chinese J. Space Sci.* , *31*(5), 607–617.

Parrot, M., and Mogilevsky, M. M. (1989). VLF emissions associated with earthquakes and observed in the ionosphere and the magnetosphere. *Phys. Earth Planet. Interi.*, *57*(1–2), 86–99. https://doi.org/10.1016/0031-9201(89)90218-5

Parrot, M., Něme, F., Santolík, O., and Berthelier, J. J. (2005). ELF magnetospheric lines observed by DEMETER. *Ann. Geophys.*, *23*(10), 3301–3311. https://doi.org/10.5194/angeo-23-3301-2005

Parrot, M. (2006). Special issue of planetary and space science 'DEMETER'. *Planet. Space Sci.*, *54*(5), 411–412. https://doi.org/10.1016/j.pss.2005.10.012

Parrot, M. (2011). Statistical analysis of the ion density measured by the satellite DEMETER in relation with the seismic activity. *Earthq. Sci.*, *24*(6), 513–521. https://doi.org/10.1007/s11589-011-0813-3

Parrot, M. (2012). Statistical analysis of automatically detected ion density variations recorded by DEMETER and their relation to seismic activity. *Ann. Geophys.*, *55*(1), 149–155. https://doi.org/10.4401/ag-5270

Píša, D., Němec, F., Parrot, M., and Santolík, O. (2012). Attenuation of electromagnetic waves at the frequency ~1.7 kHz in the upper ionosphere observed by the DEMETER satellite in the vicinity of earthquakes.. *Ann. Geophys.*, *55*(1), 157–163. https://doi.org/10.4401/ag-5276

Píša, D., Němec, F., Santolík, O., Parrot, M., and Rycroft, M. (2013). Additional attenuation of natural VLF electromagnetic waves observed by the DEMETER spacecraft resulting from preseismic activity. *J. Geophys. Res.*, *118*(8), 5286–5295. https://doi.org/10.1002/jgra.50469

Pulinets, S. A. (2009). Lithosphere-Atmosphere-Ionosphere Coupling (LAIC) model. In Hayakawa, M. (Ed.), *Electromagnetic Phenomena Associated with Earthquakes* (pp. 235–253). Kerala, India: Transworld Research Network.

Pulinets, S. A., Ouzounov, D. P., Karelin, A. V., and Davidenko, D. V. (2015). Physical bases of the generation of short-term earthquake precursors: A complex model of ionization-induced geophysical processes in the lithosphere-atmosphere-ionosphere-magnetosphere system. *Geomagn. Aeron.*, *55*(4), 521–538. https://doi.org/10.1134/S0016793215040131

Sarkar, S., Gwal, A. K., and Parrot, M. (2007). Ionospheric variations observed by the DEMETER satellite in the mid-latitude region during strong earthquakes. *J. Atmos. Sol. Terr. Phys.*, *69*(13), 1524–1540. https://doi.org/10.1016/j.jastp.2007.06.006

Shen, X. H., Zhang, X. M., Yuan, S. G., Wang, L. W., Cao, J. B., Huang, J. P., Zhu, X. H., Piergiorgio, P., and Dai, J. P. (2018). The state-of-the-art of the China Seismo-Electromagnetic Satellite mission. *Sci. China Technol. Sci.*, *61*(5), 634–642. https://doi.org/10.1007/s11431-018-9242-0

Sorokin, V. M., Chmyrev, V. M., and Hayakawa, M. (2015). *Electrodynamic Coupling of Lithosphere-Atmosphere-Ionosphere of the Earth* (pp. 326). Nova Science Pub. Inc.

Yan, R., Parrot, M., and Pinçon, J. L. (2017). Statistical study on variations of the ionospheric ion density observed by DEMETER and related to seismic activities. *J. Geophys. Res.*, *122*(12), 12421–12429. https://doi.org/10.1002/2017JA024623

Yan, R., Guan, Y. B., Shen, X. H., Huang, J. P., Zhang, X. M., Liu, C., and Liu, D. P. (2018). The Langmuir Probe onboard CSES: data inversion analysis method and first results. *Earth Planet. Phys.*, *2*(6), 479–488. https://doi.org/10.26464/epp2018046

Zeng, Z. C., Zhang, B., Fang, G. Y., Wang, D. F., and Yin, H. J. (2009). The analysis of ionospheric variations before Wenchuan earthquake with DEMETER data. *Chinese J. Geophys.* (*in Chinese*), *52*(1), 11–19.

Zeren, Z. M., Shen, X. H., Cao, J. B., Zhang X. M., Huang, J. P., Liu, J., Ouyang, X. Y., and Zhao, S. F. (2012). Statistical analysis of EIF/VI magnetic field disturbances before major earthquakes. *Chinese J. Geophys.* (*in Chinese*), *55*(11), 3699–3708. https://doi.org/10.6038/j.issn.0001-5733.2012.11.017

Zhang, X., Fidani, C., Huang, J., Shen, X., Zeren, Z., and Qian, J. (2013). Burst increases of precipitating electrons recorded by the DEMETER satellite before strong earthquakes. *Nat. Hazards Earth Syst. Sci.*, *13*(1), 197–209. https://doi.org/10.5194/nhess-13-197-2013

Zhang, X. M., Qian, J. D., Ouyang, X. Y., Shen, X. H., Cai, J. A., and Zhao, S. F. (2009a). Ionospheric electromagnetic perturbations observed on DEMETER satellite before Chile *M*7.9 earthquake. *Earthq. Sci.*, *22*(3), 251–255. https://doi.org/10.1007/s11589-009-0251-7

Zhang, X. M., Qian, J. D., Ouyang, X. Y., Cai, J. A., Liu, J., Shen, X. H., and Zhao, S. F. (2009b). Ionospheric electro-magnetic disturbances prior to Yutian 7.2 earthquake in Xinjiang. *Chinese J. Space Sci.* , *29*(2), 213–221.

Zhang, X. M., Qian, J. D., Ouyang, X. Y., Shen, X. H., Cai, J. A., and Zhao, S. F. (2009c). Ionospheric electromagnetic disturbances observed on DEMETER satellite before an earthquake of*M*7.9 in Chili. *Progress in Geophys.* , *24*(4), 1196–1203. https://doi.org/10.3969/j.issn.1004-2903.2009.04.006

Zhu, T., and Wang, L. W. (2011). LF electric field anomalies related to Wenchuan earthquake observed by DEMETER satellite. *Chinese J. Geophys.* (*in Chinese*), *54*(3), 717–727. https://doi.org/10.3969/j.issn.0001-5733.2011.03.011